Reduction of spin backflow with underlying bulk WSe₂ in Pt/Py/Al trilayers _{EP}

View Online   Export Citation   CrossMark

Kuan-Chia Chiu,[1] (iD) Yu-Hsun Chu,[1,a] (iD) and Minn-Tsong Lin[1,2,3,a] (iD)

AFFILIATIONS

[1]Department of Physics, National Taiwan University, Taipei 10617, Taiwan
[2]Institute of Atomic and Molecular Sciences, Academia Sinica, Taipei 10617, Taiwan
[3]Research Center for Applied Sciences, Academia Sinica, Taipei 11529, Taiwan

[a]Authors to whom correspondence should be addressed: yhchu@ntu.edu.tw and mtlin@phys.ntu.edu.tw

ABSTRACT

To enhance spin–orbit torque (SOT) efficiency, various approaches exist, including the modification of spin mixing conductance through interface engineering. Recent studies have highlighted that transition metal dichalcogenides with strong spin–orbit couplings serve as spin sources and sinks even in few-layer configurations. In this study, we carry out spin torque ferromagnetic resonance measurements on SOT devices with insertion of a bulk WSe₂ underlayer and reveal a notable increase in their spin mixing conductance and damping-like torque efficiency. Using the spin transparency model, we quantitatively unveil the reduction of the spin backflow factor, verifying the role of spin sink layers in SOT modification.

An electrical control of magnetization using spin–orbit torques (SOTs)[1–3] is promising for spin-based devices.[4–8] These SOTs arise from spin–orbit coupling effects like the spin Hall effect[9–12] and the Rashba–Edelstein effect[13–15] in ferromagnetic/non-magnetic metal (FM/NM) structures. The effectiveness of SOTs on the FM layer is characterized by the SOT efficiency, which is related to the spin Hall angle θ_{SH} of the NM layer and the spin transparency T at the FM/NM interface.

The backscattered spin currents from the FM/NM interface, called spin backflows, however, reduce the net spin currents acting on the FM magnetization. This backflow effect can significantly degrade the overall SOT efficiency.[16] The suppression of spin backflow is therefore crucial for realizing highly efficient SOT devices. Recent experiments have revealed approaches like utilizing spin sinks or tailoring interface properties to mitigate this detrimental spin backflow and enhance SOT.[17–19] For example, the presence of monolayer and bilayer transition metal dichalcogenides (TMDs) at the NM/FM interfaces was reported to increase spin current injection into the FM layers.[20] With large spin–orbit coupling, the 2D flakes also function as spin sinks under the NM layers and enhance the SOT efficiency.[21,22] While the enhancement leads to an idea of reduced spin backflow, it has not been evaluated in numbers. To address the roles of 2D TMDs in SOT devices, a quantitative evaluation of the spin backflow will be crucial.

In this work, we present a heterostructure consisting of WSe₂/platinum (Pt)/permalloy (Py)/aluminum (Al), with the specific goal of reducing spin backflow within the thin Pt layer. Our approach involves the utilization of spin torque ferromagnetic resonance (ST-FMR) (shown in Fig. 1)[17] as a methodology for evaluating spin transparency within the WSe₂/Pt/Py/Al heterostructure. Employing the spin transparency model, we can quantitatively estimate the spin backflow factor and examine the contribution of different interfaces in the devices.

The ST-FMR circuit [yellow part in Fig. 1(a)] is fabricated as coplanar waveguides (CPWs)[23] with ground–signal–ground (G–S–G) architecture. The fabrication process begins with photolithography on a sapphire substrate (C-plane) using a laser writer (Heidelberg DWL66). Subsequently, Cr/Au electrodes are thermally deposited with a base pressure of 2×10^{-6} mbar. The deposition rates for Cr and Au are 0.5 and 1 Å/s, respectively. The circuit dimensions are 1.6×1.25 mm².

The exfoliated WSe₂ flakes with thicknesses ranging from 10 to 30 nm were transferred onto the signal electrode, bridging the gap between the signal and ground electrodes. A further photolithography step is performed to define a rectangular bar structure. Following this, magnetron sputtering is employed to deposit Pt, Py, and Al, with a base pressure of approximately 7×10^{-8} mbar. The Pt (4 nm)/Py (8.28 nm)/Al (2 nm) resistivity is $1.4 \pm 0.2 \times 10^{-6}$ (Ω m) on WSe₂ and $1.2 \pm 0.2 \times 10^{-6}$ (Ω m) on SiO₂, which is highly insulating as the sapphire substrates. The comparable resistivity values of the trilayer structure on these substrates indicate minimal current shunting through the WSe₂ layers. The deposition rates for Pt, Py, and Al are 0.39, 0.12,
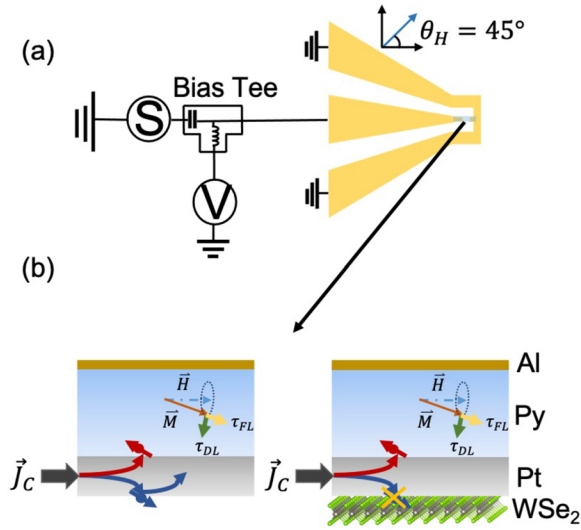
FIG. 1. (a) Schematic diagram of ST-FMR setup (b) utilizing WSe$_2$ as spin sink in WSe$_2$(bulk)/Pt(2 nm)/Py (t nm)/Al(2 nm) multilayer.

and 0.067 Å/s, respectively. Here, we need to address that Al prevents the oxidation of other layers. After fabricating the ST-FMR circuit, we connect it to G–S–G bigger electrodes with silver paste, providing a convenient connection to our radio frequency (RF) source.

The ST-FMR measurement uses a vector network analyzer (Keysight 4294A) as the microwave source. The generated spin torque-induced DC voltage is combined with the RF voltage, and to segregate the DC and AC components, a bias tee is employed. Due to the high resistivity of WSe$_2$ without external gating or doping, current does not flow into WSe$_2$. Therefore, the ST-FMR voltage is mainly from the Pt layer. To generate a larger SOT-generated voltage, we need to use higher microwave power (13 dBm). The DC component is subsequently measured using a nano-voltage meter (Keithley 2182). The applied magnetic field is oriented at 45° relative to the signal line,[24] a configuration optimized to achieve the maximum ST-FMR voltage due to largest the anisotropic magnetoresistance (AMR).

To investigate the correlation between the reduction of spin backflow and the strength of SOT efficiency with and without WSe$_2$ underlayer, we opted to explore the thickness dependence of Py. This approach allows us to extract the key SOT-related parameters, namely SOT, the damping-like torque (DLT), and the field-like torque (FLT) efficiency, along with spin-related parameters such as spin mixing conductance and spin backflow.

For assessing spin backflow, we require information on the change in spin mixing conductance. This involves identifying the FM thickness dependence of the damping constant. These parameters can be estimated through the FM thickness dependence of ST-FMR measurements. Specifically, the symmetric term, anti-symmetric term, and linewidth will be obtained through fitting ST-FMR voltages. The procedure is depicted in the flow chart in Fig. 2.

We utilize Eq. (1) to fit the bias tee voltage[17] with WSe$_2$ underlayer [Fig. 3(a)] and without WSe$_2$ underlayer [Fig. 3(b)], extracting parameters such as H_{FMR}, ΔH, the symmetric term (V_S), which is associated with the DLT, the antisymmetric term (V_A), which is linked to the FLT, and the Oersted field,
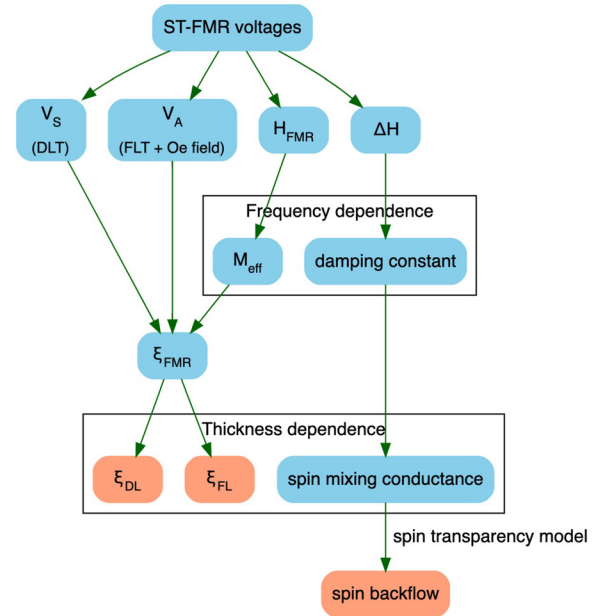
FIG. 2. The flow chart illustrates the process of extracting the final parameter ξ_{DL}, ξ_{FL}, and spin backflow. The orange rounded rectangles at the bottom of the diagram highlight these key output parameters. Key components include the symmetric Lorentzian term (V_S), antisymmetric Lorentzian term (V_A), ferromagnetic resonance field (H_{FMR}), and linewidth (ΔH) in fitting Eq. (1). Additionally, the effective magnetization (M_{eff}) is determined in Eq. (2). The torque efficiency terms are spin–orbit torque (ξ_{FMR}), damping-like torque (ξ_{DL}), and field-like torque (ξ_{FL}) describing the relationship in Eq. (6).

$$V(H_{ext}) = V_S \cdot \frac{\Delta H^2}{\Delta H^2 + (H_{ext} - H_{FMR})^2} + V_A \cdot \frac{\Delta H(H_{ext} - H_{FMR})}{\Delta H^2 + (H_{ext} - H_{FMR})^2}.$$
(1)

Equation (2) is shown to be consistent with the Kittel formula[25] and acquires the effective magnetization (M_{eff}), describing the relationship between microwave frequencies and resonance field, where f and γ denote the microwave frequency and gyromagnetic ratio γ, respectively,

$$f = \frac{\gamma}{2\pi} \sqrt{H_{FMR}(H_{FMR} + 4\pi M_{eff})}.$$
(2)

The effective magnetizations obtained from fitting are 7178.68 Oe with the inclusion of WSe$_2$ and 5943.37 Oe without WSe$_2$, as shown in Fig. 3(c). The increased M_{eff} might result from smoother thin films grown on the WSe$_2$ surfaces.[26]

In Eq. (1), V_S and V_A are related to the DLT and FLT efficiency as follows:[27]

$$V_S = \frac{\hbar}{2e} \frac{\xi_{DL} J_e^{rf}}{4\pi M_s t_{FM}^{eff}},$$
(3)

$$V_A = \left(\frac{\hbar}{2e} \frac{\xi_{FL} J_e^{rf}}{4\pi M_s t_{FM}^{eff}} + \frac{J_e^{rf} d_{NM}}{2} \right) \sqrt{1 + (4\pi M_{eff}/H_{FMR})},$$
(4)

where e, $\hbar$, t_{FM}^{eff}, d_{NM}, and J_e^{rf} are the elementary charge, Planck's constant, effective thickness of the FM layer, thickness of the NM layer,

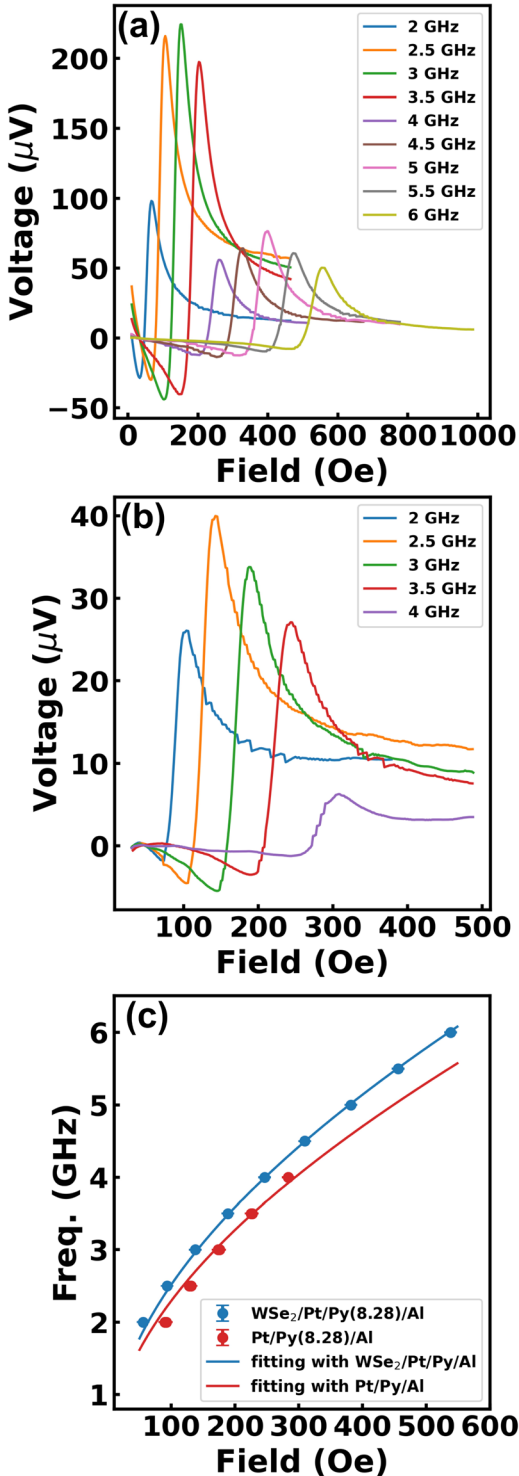**FIG. 3.** (a) Frequency dependence of WSe$_2$/Pt (2 nm)/Py (8.28 nm)/Al (2 nm) sample; (b) frequency dependence of Pt (2 nm)/Py (8.28 nm)/Al (2 nm) sample; (c) the relation between frequencies and resonance fields. The solid lines represent the fitting from Eq. (2).

and radio frequency current on the electrode, respectively. The saturation magnetization M_s of Py is 805 emu/cm^3 measured by a vibrating-sample magnetometer (VSM).

$$\xi_{\text{FMR}} = \frac{V_S}{V_A}\frac{e}{\hbar}4\pi M_s \cdot t_{\text{FM}}^{\text{eff}} \cdot d_{\text{NM}}\sqrt{1 + (4\pi M_{\text{eff}}/H_{\text{FMR}})} \quad (5)$$

is the SOT efficiency.[27] It serves as the parameter defining the strength of spin-to-charge conversion, interacting with various torques, such as the DLT, FLT, and Oersted field. ξ_{FMR} changes with variations in the thickness of the FM layer due to the field $h_{\text{FLT}} = \frac{\hbar}{2e}\frac{\xi_{\text{FL}}J_e^{\text{rf}}}{4\pi M_s t_{\text{FM}}^{\text{eff}}}$ in Eq. (4).[27] To provide a more precise description of SOT efficiency across different FM or NM thicknesses, the modified relationship should follow Eq. (6). This revision separates ξ_{FMR} into ξ_{DL} and ξ_{FL}. It is essential to note that ξ_{FMR} is not power dependent since V_S/V_A to normalize the varying microwave current at different frequencies due to slight variations of power absorption from the CPWs as well as frequency-dependent power decay. Our measurement approach involves analyzing the correlation between the SOT efficiency and the thickness of the FM layer. This method allows us to extract the DLT and FLT efficiency by assessing the thickness dependence of the FM using Eqs. (5) and (6),[27]

$$\frac{1}{\xi_{\text{FMR}}} = \frac{1}{\xi_{\text{DL}}}\left(1 + \frac{\hbar}{e}\frac{\xi_{\text{FL}}}{4\pi M_{\text{eff}} \cdot t_{\text{FM}}^{\text{eff}} \cdot d_{\text{NM}}}\right). \quad (6)$$

The intercept of this fit provides the value $1/\xi_{\text{DL}}$, while the slope is directly proportional to $1/\xi_{\text{FL}}$ shown in Fig. 4. For samples incorporating WSe$_2$, we determined the DLT efficiency to be 0.28 ± 0.25 and the FLT efficiency to be 0.05 ± 0.06, resulting in an R-squared value (R^2) of 0.91. In contrast, for the control sample without WSe$_2$, the DLT efficiency was measured at 0.16 ± 0.12, and the FLT efficiency was found to be 0.04 ± 0.04, yielding an R-squared value of 0.96. These results indicate that the insertion of a WSe$_2$ underlayer led to an

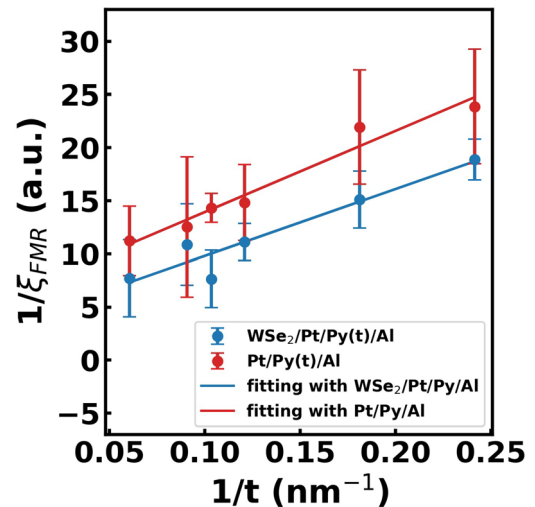**FIG. 4.** Inverse Py thickness dependence, $1/t$, of inverse SOT efficiency $1/\xi_{\text{FMR}}$. The solid lines represent fitting curves based on Eq. (6). The data are plotted using the inverse scale for convenient analysis.

enhancement in the DLT efficiency, while the FLT efficiency showed minimal change. The similar FLT values suggest consistent interfaces between the Pt and the Py layers since the FLT is largely contributed by the interfacial Rashba effect.[28]

On the other hand, we can utilize the same ST-FMR voltages to fit the spin mixing conductance by thickness dependence of FM. Since the damping constant (α) can be extracted from the frequency dependence of linewidths (ΔH), deriving the value using Eq. (7),[25] which are within a reasonable range of damping constants for Py films of similar thickness.[29]

$$\Delta H = \Delta H_{ext} + \frac{2\pi\alpha}{\gamma}f. \tag{7}$$

The representation of spin mixing conductance relies on the slope derived from the inverse thickness dependence of the FM layers in the following equation,[19] in which the damping constant varies with the FM thickness (t_{FM}^{eff}) and G_{eff} is the effective spin mixing conductance:

$$\alpha = \alpha_0 + \frac{2\pi\gamma\hbar^2 G_{eff}^{\uparrow\downarrow}}{e^2 M_s}\frac{1}{t_{FM}^{eff}}. \tag{8}$$

The damping constants are smaller with the WSe$_2$ underlayer, which may result from reduced intrinsic damping constant α_0 due to smoother film growths on WSe$_2$ flakes. To further confirm the spin injection, we need to do thickness dependence of FM layers from damping constant. Figure 5(b) represents the inverse thickness dependence of the damping constant, with the blue fitting having an R^2 value of 0.965 and the red fitting yielding an R^2 value of 0.976. The fitting gives the effective spin mixing conductance as $G_{WSe_2} = 2.9 \pm 0.4 \times 10^{14}$ (Ω^{-1} m^{-2}) with WSe$_2$ and $G_{sapphire} = 2.4 \pm 0.4 \times 10^{14}$ (Ω^{-1} m^{-2}) without WSe$_2$. Notably, we observed an increase in spin mixing conductance upon introducing the WSe$_2$ layer. It should be noted that the two magnon scattering (TMS) contribution can be estimated by adding a $\left(1/t_{FM}^{eff}\right)^2$ term to Eq. (8), from which our fitting result shows that the TMS contribution is negligible. On the other hand, it can be seen that ΔH_{ext} of the WSe$_2$-based sample is slightly larger in Fig. 5(a), while the film inhomogeneity should be reduced via smoother growths on WSe$_2$. We suspect that the low thermal conductivity of WSe$_2$ causes local temperature variations during measurements and is responsible for the broadened linewidths.[30,31] To estimate the reduction in spin backflow and explain the increasing spin mixing conductance, we can employ a straightforward spin transparency model described in Fig. 6.[32]

As shown in Fig. 6, Py exhibits an intrinsic damping term α_{int}. When a spin current passes through the interface, it encounters spin memory loss due to scattering. Subsequently, there is a spin mixing resistance $\frac{1}{G_{Py/Pt}^{\uparrow\downarrow}}$ across Py to Pt. Finally, the dissipation in Pt is characterized by $\frac{1}{G_{Pt}}$. In this model, the effective spin resistance of Pt is influenced by WSe$_2$ and the sapphire substrate, altering the spin backflow. The spin transparency (T) is defined as $(1-\delta)\cdot\varepsilon$,[19] where δ represents the spin relaxation factor at the interface, and ε is the spin backflow factor in the NM layer. This T measures the ease with which spin can traverse through all the layers. The reduction of T enhances spin injection into adjacent layers. The introduction of WSe$_2$ is aimed at diminishing spin backflow. We assume that spin relaxation remains constant at the Pt/Py interfaces due to the unchanged FLT efficiency.
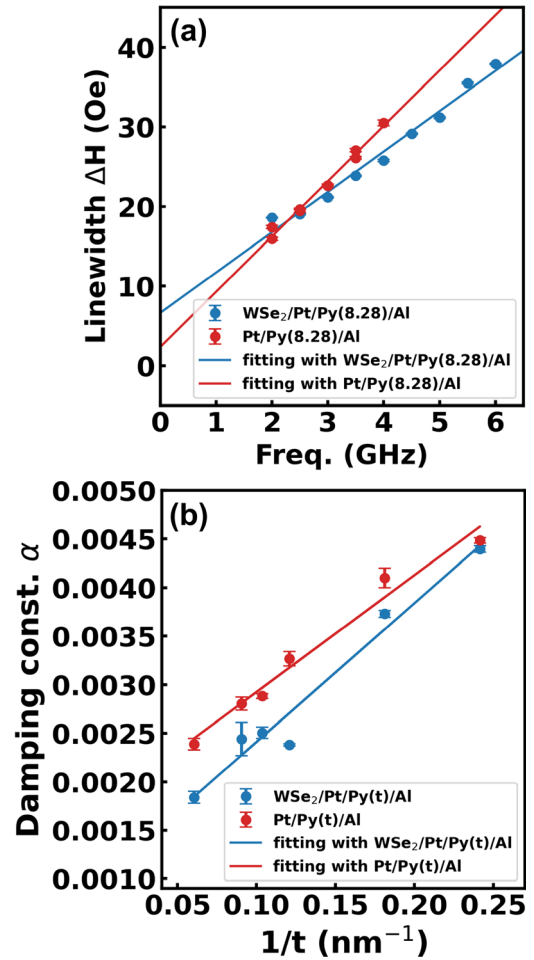

FIG. 5. (a) The slope of linewidth vs frequency indicates the strength of the damping constant. The solid lines represent fitting curves based on Eq. (7). (b) Py thickness dependence of damping constant can estimate the effective spin mixing conductance. The solid lines represent fitting curves based on Eq. (8).

The spin backflow of Pt on sapphire can be computed as $\varepsilon_{sapphire} = \frac{1/G_{Pt}}{1/G_{Pt}+1/G_{Py/Pt}^{\uparrow\downarrow}} = 0.983 \pm 0.004$.[19] Here, the spin conductance is defined by $G_{Pt} = \frac{\tanh(t_{Pt}/\lambda_{Pt})}{2\rho_{Pt}\cdot\lambda_{Pt}} = 0.21 \pm 0.01 \times 10^{14}$ (Ω^{-1} m^{-2}), with λ_{Pt} being 4 nm,[33] and the spin mixing conductance $G_{Py/Pt}^{\uparrow\downarrow}$ is $12 \pm 2 \times 10^{14}$ (Ω^{-1} m^{-2}).[33] Using the effective spin mixing conductance[34] $G_{sapphire} = G_{Py/Pt}^{\uparrow\downarrow}[1-(1-\delta)^2\cdot\varepsilon_{sapphire}]$, we calculate δ to be 0.10 ± 0.03. Subsequently, we use δ and G_{WSe_2} to obtain $\varepsilon_{WSe_2} = 0.76 \pm 0.06$.

Our model suggests that inserting WSe$_2$ may change the effective spin resistance of Pt ($1/G_{Pt}$), consequently reducing spin backflow, which explains the observed increase in effective spin mixing conductance $G_{eff} = G_{Py/Pt}^{\uparrow\downarrow}[1-(1-\delta)^2\cdot\varepsilon]$. Our analysis demonstrates a reduction in spin backflow ε_{WSe_2} (0.76) compared to $\varepsilon_{sapphire}$ (0.98) when introducing WSe$_2$, resulting in enhanced spin injection. This is accompanied by an improvement in the DLT efficiency, rising from 0.16 to 0.28 compared to the pristine system. It has been reported that
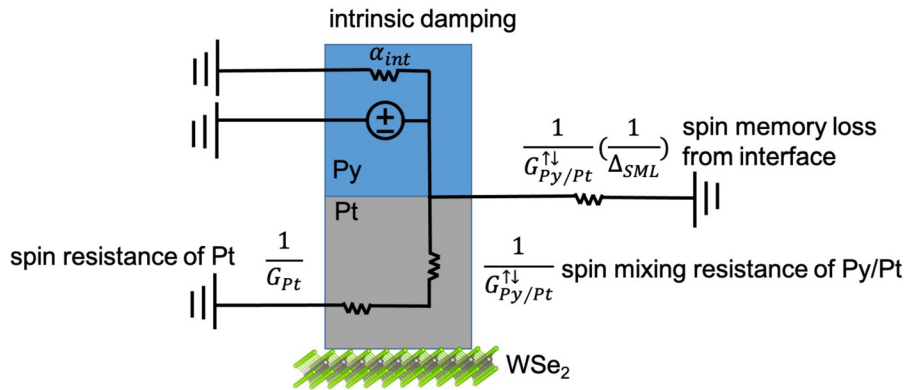
FIG. 6. The circuit model represents the angular momentum flow driven by FMR excitation in the WSe_2/Pt/Py trilayer. Spin current is distributed among parallel resistance channels arising from spin pumping into the Py seed and Pt spin sink layers, alongside spin memory loss. Moreover, the spin resistance of Pt is directly linked to the spin backflow factor.[32]

TABLE I. Results of Pt/Py/Al and WSe_2/Pt/Py/Al films from fitted ST-FMR spectrum and spin transparency model: G_{eff} is the spin mixing conductance, ε is the backflow factor, T is the spin transparency, ξ_{DL} is the DLT efficiency, and ξ_{FL} is the FLT efficiency. The estimated values are obtained directly from the figures in Refs. 22 and 35.

Sample	$G_{eff}(\times 10^{14}\,\Omega^{-1}\,m^{-2})$	$\varepsilon(\times 10^{-2})$	$T(\times 10^{-2})$	$\xi_{DL}(\times 10^{-2})$	$\xi_{FL}(\times 10^{-2})$	Reference
Pt/Py/Al	2.4 ± 0.4	98.3 ± 0.4	88 ± 3	16 ± 16	4 ± 4	This work
WSe_2(bulk)/Pt/Py/Al	2.9 ± 0.4	76.0 ± 6	68 ± 7	28 ± 25	5 ± 6	This work
Pt/Co	9.9	$\cdots$	32	42 ± 7	26 ± 25	19
Pt/TiN/Co	6.4	$\cdots$	53	18 ± 4	5 ± 19	19
Py/Pt	$\cdots$	$\cdots$	~ 69	9.0 ± 0.4	2.4 ± 0.3	35
Py/NiO (0.6 nm)/Pt	$\cdots$	$\cdots$	~ 82	~ 10	~ 3	35
Pt/Co/AlO$_x$	$\cdots$	$\cdots$	$\cdots$	~ 6.2	$\cdots$	22
WSe_2(5ML)/Pt/Co/AlO$_x$	$\cdots$	$\cdots$	$\cdots$	~ 14.1	$\cdots$	22

the spin transparency and the DLT and FLT efficiencies can be adjusted via interfacial modifications at the FM/NM interfaces. An insertion layer could improve or suppress spin injections depending on the material choices, and generally, both the DLT and FLT efficiencies are influenced, as shown in the work of Moriya *et al.*[19] and Dong *et al.*[35] in Table I. A structure with underlayer spin sinks has been reported in the work of Xue *et al.*[22] (in Table I) in which the spin backflow factor and the FLT efficiency were not acquired. Using a different methodology, including the spin transparency model, we quantified spin transparency, spin backflow, and the DLT as well as FLT efficiencies. The unaltered FLT efficiency indicates a negligible additional Py/Pt and Pt/WSe_2 interfacial SOT contribution, such as the Rashba effect, agreeing with spin injection enhancement from the spin sink, and thereby selectively controlling spin torque efficiencies. The approach utilizing an underlayer signifies a distinct strategy compared to FM/NM interface engineering and allows for a more comprehensive understanding of future underlayer engineering.

In conclusion, our study demonstrates the enhancement of spin mixing conductance through a bulk WSe_2 underlayer, while maintaining a consistent interface state and unaltered FLT efficiency. Analysis of the ST-FMR spectra revealed an increase in spin mixing conductance (from 2.41 to $2.85 \times 10^{14}\,\Omega^{-1}\,m^{-2}$). Notably, the DLT efficiency improved significantly from 0.16 to 0.28, which is a 75% increase, whereas the FLT efficiency showed minimal change. This selective enhancement of the DLT is linked to effective reduction of the spin backflow, which is a 22.7% decrease quantitatively evaluated through the spin transparency model. These findings offer valuable insights for optimizing spin-based devices by mitigating spin backflow without perturbing the interface, with significant implications for future spin–orbit torque research.

AUTHOR DECLARATIONS
Conflict of Interest

The authors have no conflicts to disclose.

Author Contributions

Kuan-Chia Chiu: Conceptualization (equal); Formal analysis (equal); Investigation (lead); Visualization (lead); Writing – original draft (lead); Writing – review & editing (equal). **Yu-Hsun Chu:** Formal analysis (equal); Supervision (equal); Writing – review & editing (equal). **Minn-Tsong Lin:** Conceptualization (equal); Funding acquisition (equal); Resources (equal); Supervision (equal); Writing – review & editing (equal).

DATA AVAILABILITY

The data that support the findings of this study are available from the corresponding authors upon reasonable request.

REFERENCES

[1] L. Liu, C.-F. Pai, Y. Li, H. W. Tseng, D. C. Ralph, and R. A. Buhrman, Science **336**, 555 (2012).

[2] N. Locatelli, V. Cros, and J. Grollier, Nat. Mater. **13**, 11 (2014).

[3] Q. Shao, P. Li, L. Liu, H. Yang, S. Fukami, A. Razavi, H. Wu, K. Wang, F. Freimuth, Y. Mokrousov, M. D. Stiles, S. Emori, A. Hoffmann, J. Åkerman, K. Roy, J.-P. Wang, S.-H. Yang, K. Garello, and W. Zhang, IEEE Trans. Magn. **57**, 800439 (2021).

[4] S.-W. Lee and K.-J. Lee, Proc. IEEE **104**, 1831 (2016).

[5] D. Apalkov, B. Dieny, and J. M. Slaughter, Proc. IEEE **104**, 1796 (2016).

[6] T. Endoh, H. Honjo, K. Nishioka, and S. Ikeda, in *IEEE Symposium on VLSI Technology* (IEEE, 2020).

[7] A. A. Awad, P. Dürrenfeld, A. Houshang, M. Dvornik, E. Iacocca, R. K. Dumas, and J. Åkerman, Nat. Phys. **13**, 292–299 (2017).

[8] J. Zhou and J. Chen, Adv. Electron. Mater. **7**, 2100465 (2021).

[9] M. I. Dyakonov and V. I. Perel, Phys. Lett. A **35**, 459 (1971).

[10] Y. K. Kato, R. C. Myers, A. C. Gossard, and D. D. Awschalom, Science **306**, 1910 (2004).

[11] S. O. Valenzuela and M. Tinkham, Nature **442**, 176 (2006).

[12] J. Sinova, S. O. Valenzuela, J. Wunderlich, C. H. Back, and T. Jungwirth, Rev. Mod. Phys. **87**, 1213 (2015).

[13] V. M. Edelstein, Solid State Commun. **73**, 233 (1990).

[14] A. Manchon, H. C. Koo, J. Nitta, S. M. Frolov, and R. A. Duine, Nat. Mater. **14**, 871 (2015).

[15] M.-G. Kang, J.-G. Choi, J. Jeong, J. Y. Park, H.-J. Park, T. Kim, T. Lee, K.-J. Kim, K.-W. Kim, J. H. Oh, D. D. Viet, J.-R. Jeong, J. M. Yuk, J. Park, K.-J. Lee, and B.-G. Park, Nat. Commun. **12**, 7111 (2021).

[16] H. Jiao and G. E. W. Bauer, Phys. Rev. Lett. **110**, 217602 (2013).

[17] L. Liu, T. Moriyama, D. C. Ralph, and R. A. Buhrman, Phys. Rev. Lett. **106**, 036601 (2011).

[18] A. Kumar, R. Sharma, K. I. Ali Khan, C. Murapaka, G. J. Lim, W. S. Lew, S. Chaudhary, and P. K. Muduli, ACS Appl. Electron. Mater. **3**, 3139 (2021).

[19] H. Moriya, A. Musha, and K. Ando, Appl. Phys. Express **14**, 063001 (2021).

[20] S. Novakov, B. Jariwala, N. M. Vu, A. Kozhakhmetov, J. A. Robinson, and J. T. Heron, ACS Appl. Mater. Interfaces **13**, 13744 (2021).

[21] P. Debashis, T. Y. T. Hung, and Z. Chen, npj 2D Mater. Appl. **4**, 18 (2020).

[22] H. Xue, M. Tang, Y. Zhang, Z. Ji, X. Qiu, and Z. Zhang, Adv. Electron. Mater. **8**, 2100684 (2022).

[23] I. S. Maksymov and M. Kostylev, Physica E **69**, 253 (2015).

[24] Y. Wang, R. Ramaswamy, and H. Yang, J. Phys. D **51**, 273002 (2018).

[25] C. Kittel, Phys. Rev. **73**, 155 (1948).

[26] M. Li, G.-C. Wang, and H.-G. Min, J. Appl. Phys. **83**, 5313 (1998).

[27] C.-F. Pai, Y. Ou, L. H. Vilela-Leão, D. C. Ralph, and R. A. Buhrman, Phys. Rev. B **92**, 064426 (2015).

[28] V. P. Amin and M. D. Stiles, Phys. Rev. B **94**, 104420 (2016).

[29] Y. Zhao, Q. Song, S.-H. Yang, T. Su, W. Yuan, S. S. P. Parkin, J. Shi, and W. Han, Sci. Rep. **6**, 22890 (2016).

[30] B. Wang, X. Yan, H. Yan, and Y. Cai, Nanotechnology **33**, 275706 (2022).

[31] S. He and C. Panagopoulos, Rev. Sci. Instrum. **87**, 043110 (2016).

[32] A. J. Berger, E. R. J. Edwards, H. T. Nembach, O. Karis, M. Weiler, and T. J. Silva, Phys. Rev. B **98**, 024402 (2018).

[33] V. Vlaminck, J. E. Pearson, S. D. Bader, and A. Hoffmann, Phys. Rev. B **88**, 064414 (2013).

[34] K. Chen and S. Zhang, IEEE Magn. Lett. **6**, 3000304 (2015).

[35] J. Dong, C. Cheng, J. Wei, H. Xu, Y. Zhang, Y. Wang, Z. Zhu, L. Li, H. Wu, G. Yu, and X. Han, Appl. Phys. Lett. **122**, 122401 (2023).